Draft version November 14, 2025
Typeset using LaTeX **twocolumn** style in AASTeX631

Systematic Analysis of Changing-look AGN Variability Using ZTF Light Curves

Huimei Wang [1,2] Xue-Bing Wu [1,2] Nanyu Yao,[1] Bing Lyu [1,2] Yuxuan Pang [1,2] Yuming Fu [3,4]
Rui Zhu [1,2] and Qian Yang [5]

[1] *Department of Astronomy, School of Physics, Peking University, Beijing 100871, People's Republic of China*
[2] *Kavli Institute for Astronomy and Astrophysics, Peking University, Beijing 100871, People's Republic of China*
[3] *Leiden Observatory, Leiden University, Einsteinweg 55, 2333 CC Leiden, The Netherlands*
[4] *Kapteyn Astronomical Institute, University of Groningen, P.O. Box 800, 9700 AV Groningen, The Netherlands*
[5] *Center for Astrophysics — Harvard & Smithsonian, 60 Garden Street, Cambridge, MA 02138, USA*

ABSTRACT

Changing-look active galactic nuclei (CLAGNs) are a unique population of AGNs that exhibit the appearance (turn-on) or disappearance (turn-off) of broad emission lines. This study aims to explore the intrinsic mechanisms of CLAGNs by investigating their photometric variability using data from the Zwicky Transient Facility (ZTF), which has provided high-cadence observations over the past five years. By visual inspections, we construct a sample of 152 CLAGNs from the literature, all of which show spectral transitions and large optical variability in their ZTF light curves. By analyzing 90 of these CLAGNs and the control samples of Type 1 AGNs, Type 2 AGNs, and extremely variable quasars (EVQs), matched in redshift ($0.2 < z < 0.8$) and supermassive black hole mass, we compare the color variability, structure function (SF), and variability metric σ_{QSO}, which quantifies how closely the light curves resemble a damped random walk (DRW) model. We find that while CLAGNs and EVQs differ from typical Type 1 and Type 2 AGNs in bolometric luminosity and Eddington ratio, the on/off-state CLAGNs share similar variability patterns with the overall CLAGN population, and distinct from EVQ, Type 1 and Type 2 AGNs. This suggests that 'on' and 'off' CLAGNs are not simply equivalent to Type 1 and Type 2 AGNs, respectively. Instead of undergoing genuine transitions between two AGN types, CLAGNs may inhabit a critical state where moderate fluctuations in accretion rate lead to the temporary spectral changes.

Keywords: Active galactic nuclei (16); Quasars (1319); Photometry (1234); Light curves (918)

1. INTRODUCTION

Active Galactic Nuclei (AGNs) are among the most luminous and dynamic objects in the Universe, powered by accretion onto super-massive black holes (SMBHs) at the centers of galaxies. AGNs are classified into Type 1 and Type 2 AGNs based on their emission line features. Type 1 AGNs show broad and narrow emission lines, while Type 2 AGNs only show narrow emission lines. In the unified model of AGNs, the difference in viewing angle affect the obscuration of the broad line region (BLR) by the dusty torus and cause the difference between Type 1 and Type 2 AGNs (Urry & Padovani 1995).

Corresponding author: Huimei Wang
wang_hm@pku.edu.cn

wuxb@pku.edu.cn

Changing-look active galactic nuclei (CLAGNs) refer to a special type of AGNs that exhibit significant spectral changes, characterized by the appearance or disappearance of broad emission lines. Most of these objects also exhibit large amplitude changes in luminosity (MacLeod et al. 2019). Over the past decades, with the accumulation of large-scale spectroscopic survey data, the number of identified CLAGNs has increased significantly, with approximately 1000 CLAGNs discovered to date (Yang et al. 2018; MacLeod et al. 2019; Sheng et al. 2020; Potts & Villforth 2021; Jin et al. 2022; Yang et al.

2023; Guo et al. 2024, 2025; Dong et al. 2025). It is generally believed that the spectral type transitions in CLAGNs are primarily driven by three mechanisms: (1) tidal disruption events (van Velzen et al. 2020), (2) obscuration by intervening clouds (Mereghetti et al. 2021), and (3) intrinsic changes in accretion rate (LaMassa et al. 2015; MacLeod et al. 2016; Graham et al. 2020; Yang et al. 2023). The majority of CLAGN transitions are thought to be caused by intrinsic variations in the accretion rate (Ricci & Trakhtenbrot 2023), although the exact physical mechanism behind these changes remains unclear.

The variability is a signature of quasars across all wavelengths and timescales. In the rest-frame UV and optical bands, the continuum emission from the accretion disc of quasars typically varies about 0.2 mag at a time scale of days to years (Vanden Berk et al. 2004; MacLeod et al. 2012). MacLeod et al. (2019) found that CLAGNs have larger variability than typical AGNs. Ren et al. (2022) found that extremely variable quasars (EVQs), with large optical photometric variability, lie in the tail of a broad distribution of quasar properties, and are not a distinct population, similar to CLAGNs, though EVQs do not exhibit the dramatic emergence or disappearance of broad emission lines. However, it is yet unclear whether the variability in CLAGNs and normal AGNs are driven by the same mechanisms.

While many studies have focused on the spectral transitions of CLAGNs, understanding their variability in photometric data, such as color and magnitude changes, is equally important (MacLeod et al. 2012). Photometric variability studies can reveal additional insights about the accretion process and the nature of transition between Type 1 to Type 2 states. Kovacevic et al. (2025) compares the optical variability of Seyfert 1 and Seyfert 2 AGNs in the Swift BAT sample using TESS and ASAS-SN light curves. It was found that Seyfert 1s exhibit significantly stronger variability, supporting the orientation-based unification models. Thus, it is worth building large samples of CLAGNs and EVQs, to explore whether they have different variability properties from normal Type 1 and Type 2 AGNs.

In this study, we plan to investigate the color variability, structure function, and variability metric of CLAGNs using data from the Zwicky Transient Facility (ZTF). ZTF is an ongoing time-domain photometric survey started in 2018, designed to monitor the entire northern sky. This survey utilizes a wide-field camera mounted on the Samuel Oschin Telescope at Palomar Observatory, and provide public data releases (DR) that offer relatively deep photometric light curves, with a g-band limiting magnitude of 20.8 mag (Masci et al. 2019). ZTF is notable for its high cadence, capturing observations approximately every 3 days, which is crucial for studying the rapid variability of astronomical objects, including a large sample of AGNs (Wang et al. 2024).

We compile a sample of CLAGNs and a corresponding control sample composed of Type 1 AGNs, Type 2 AGNs, and EVQs, matched in redshift and black hole mass. By comparing CLAGNs with Type 1 and Type 2 AGNs, as well as EVQs, we aim to determine whether the variability mechanisms in CLAGNs are distinct from those of other AGNs or they share common origins.

This paper is organized as follows. We describe the data and sample selection in Section 2. Results and discussions are given in Section 3 and 4, respectively. Throughout this paper, we adopt a standard ΛCDM cosmology with $\Omega_\Lambda = 0.7$, $\Omega_m = 0.3$, and $H_0 = 70\,\mathrm{km\,s^{-1}\,Mpc^{-1}}$.

2. DATA

2.1. *ZTF lightcurve*

We extract ZTF DR23 [1] light curves for quasars in our final sample in the g-band and r-band. The ZTF DR23 has light curves up to 6 years in length with yearly gaps. We also exclude bad measurements where the `catflags` parameter is not zero, and remove significant outliers that deviate by more than 3σ from the local median. We also perform a 3-day binning to reduce scatter.

2.2. *Changing-look AGN Sample*

To date, the number of optical CLAGNs found based on various methods is about 300. There are mainly two methods to select CLAGNs: 1) repeat spectra (e.g. Sloan Digital Sky Survey (SDSS, Pâris et al. (2018)), Dark Energy Spectroscopic Instrument spectra (DESI, DESI Collaboration et al. (2025)), Large Sky Area Multi-Object Fiber Spectroscopic Telescope (LAMOST, Cui et al. (2012))) in different or multi-epoch spectral surveys (López-Navas et al. 2023; Potts & Villforth 2021; Yang et al. 2023; Zeltyn et al. 2024); 2) photometric variability and follow-up spectroscopic observations (Yang et al. 2018; Sheng et al. 2020; MacLeod et al. 2019; Yang et al. 2025). Both of these method often involve visual inspection as the last step. Table 1 lists some typical photometric and spectroscopic criteria to find CLAGN candidates.

Although the appearance or disappearance of broad emission lines is widely used to define CLAGNs, and various quantitative selection criteria have been proposed, visual inspection has remained the most commonly used

[1] https://www.ztf.caltech.edu/ztf-public-releases.html

Table 1. Overview of CLAGN searching. The upper part show the sources found by photometric change, and the lower part show the sources found by spectroscopic change. For the same series of papers finding CLAGNs, we only show the latest work and the criterion.

Reference	Band	Photometric Selection Criteria
Yang et al. (2018)	Optical + Infrared	turn on: $\Delta W1 < -0.2$ and $\Delta(W1-W2) > 0.1$; Δg<0 and g<19 [a]
		turn off: $\Delta W1 > 0.2$ and $\Delta(W1-W2) < -0.1$; $\Delta g > 1$
MacLeod et al. (2019)	Optical	$\|\Delta g\| > 1$ mag, $\|\Delta r\| > 0.5$ mag (σ< 0.15 mag)[b]
Sheng et al. (2020)	Infrared	$\Delta W1 > 0.4$ and $\Delta W2 > 0.4$ at $> 5\sigma$ significance,
		max$(W1-W2) > 0.4$ and min$(W1-W2)$<0.8
Yang et al. (2025)	Optical + Infrared	$\Delta W1$, $\Delta W2 > 0.2$, $SN_{W1} > 5$, $SN_{W2} > 5$ and $SN_g > 4$[c]
Reference	**Parameter**	**Spectral Criteria**
MacLeod et al. (2019)	Flux+S/N	$N_\sigma(\lambda) > 3$; $N_\sigma(\lambda) = (f_{bright} - f_{faint})/\sqrt{\sigma^2_{bright} + \sigma^2_{faint}}$
Potts & Villforth (2021)	Flux	$\|\Delta f_\lambda\|$ show multiple CLQ feature in Hα, Hβ or continuum[d]
López-Navas et al. (2023)	Equivalent width (EW)	$> 3\sigma$ change in the EW of broad Hα and the Hα/[S ii] ratio
Yang et al. (2023)	Flux+S/N	same with MacLeod et al. (2019)
Zeltyn et al. (2024)	Flux+S/N	C (line) ≡ F2/F1 - Δ(F2/F1), max[C (line)] > 2
Yang et al. (2025)	Flux	$f_{\rm line,faint}/f_{\rm line,bright} < 0.3$

[a] $W1$ and $W2$ are bands centered at wavelengths of 3.4, 4.6 μm observed by the Wide-field Infrared Survey Explorer (WISE). g is g-band magnitude from PS1, or DELS when available, or SDSS.
[b] g and r are magnitudes from SDSS and PS1 measurements.
[c] intrinsic variability SN=$\sigma_{\rm band}/\Delta\sigma_{\rm band}$, g is g-band magnitude from ZTF lightcurves.
[d] The difference spectrum $|\Delta f_\lambda| = |f_{epoch2} - f_{epoch1}|$.

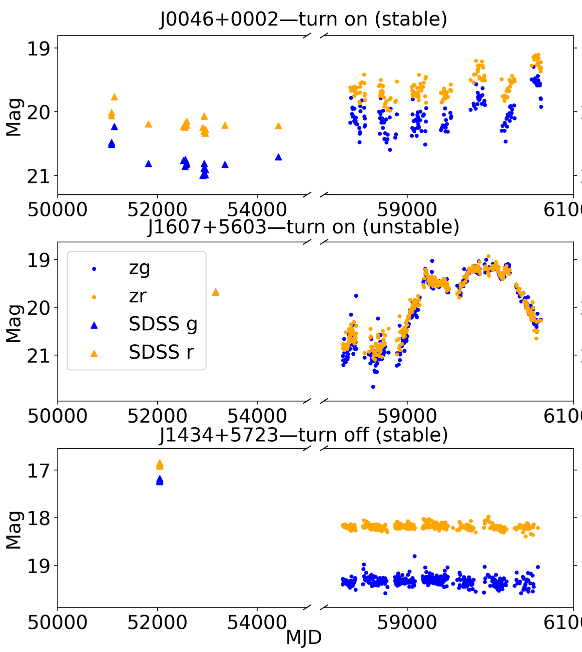

Figure 1. Light curves of three CLAGN sources in different states: (a) turn-on and recently stable, (b) turn-on and recently unstable, (c) turn-off and recently stable. ZTF g- and r-band measurements are shown as blue and orange points, while SDSS measurements are shown as blue and orange triangles, respectively. The legend in (b) is the same for (a) and (c).

as the final criterion in confirming CLAGN candidates. In this work, we collect the CLAGNs from literatures that present the spectra in multiple phases. We perform a strict visual inspection for CLAGN identification. For sources where both Hα and Hβ are covered, a source is classified as a CLAGN only if both lines fully appear or disappear between the bright and faint states (SNR $> 3\sigma$ at bright state and $< 1\sigma$ at faint state), effectively excluding most intermediate-type AGNs (e.g., Type 1.5–1.9). Among the objects where only Hβ is covered (Hα is out of optical band), some might be Type 1.9s in their dim state. These sources are conservatively treated as Type 2 in our analysis.

Table 2 lists the number of CLAGNs from literature, and Table 5 shows the details of all collected CLAGNs. We collect 228 CLAGNs in total, in which 160 of them have SMBH mass, bolometric luminosity and Eddington ratio measurements from Wu & Shen (2022); Yang et al. (2025). Among them, 152 sources have redshift $z <$ 0.8 to ensure the Hα or Hβ observations in the optical spectra.

2.3. *Control Sample*

We construct a control sample consisting of Type 1 AGNs, Type 2 AGNs, and extremely variable quasars (EVQs) with the same physical parameters including redshift and SMBH mass with our CLAGNs to compare the photometric variability between CLAGNs and the control samples. For all kinds of control sample, we

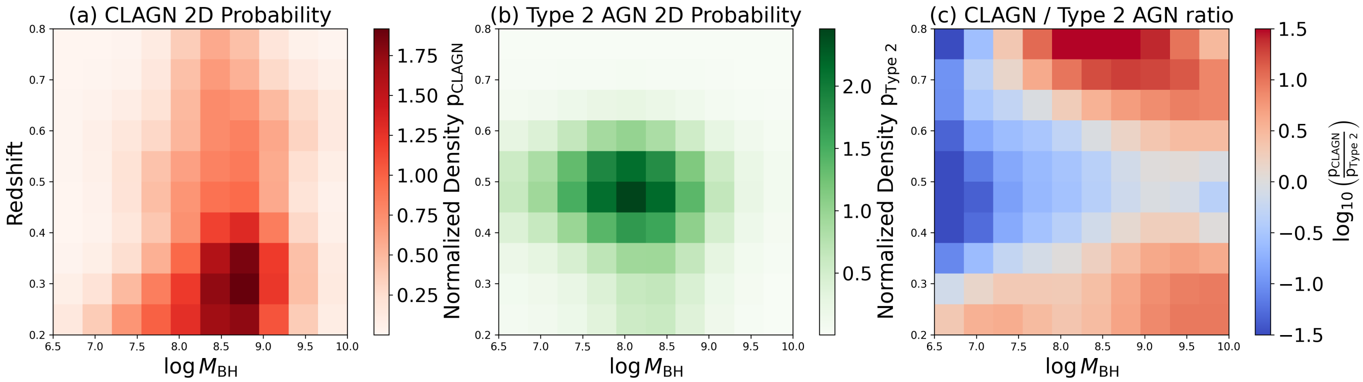

Figure 2. Two-dimensional distributions of CLAGNs (a) and Type 2 AGNs (b) in the $\log M_{\rm BH}$–z plane, and their logarithmic ratio (panel c). These distributions are used to construct a control sample of Type 2 AGNs matched to the CLAGNs in both dimensions via the probability-based sampling. Type 2 sample exhibits lower source density near all four corners of the 2D parameter space, resulting in larger sampling uncertainties and stronger deviations in the ratio.

Table 2. Number of CLAGNs from literature.

Reference	Number
Zeltyn et al. (2024)	72
Yang et al. (2025)	70
Yang et al. (2018)	26
MacLeod et al. (2019)	17
MacLeod et al. (2016)	10
López-Navas et al. (2023)	9
Sheng et al. (2020)	6
Frederick et al. (2019)	6
López-Navas et al. (2022)	4
Potts & Villforth (2021)	4
Yang et al. (2023)	4

limit the redshift z<0.8, to ensure spectroscopic coverage in the observed Hβ or Hα wavelength windows.

EVQs are a population of sources that exhibit large optical photometric variability, with CLAGNs potentially comprising a subsample (Ren et al. 2022). These EVQs were selected by the criterion: $|\Delta g_{\rm max}| > 1$ mag and $|\Delta r_{\rm max}| > 0.8$ mag where $|\Delta g_{\rm max}|$ and $|\Delta r_{\rm max}|$ represent the maximum differences in g- and r-band magnitudes between any two epochs in the light curves. MacLeod et al. (2019) adopted a similar selection to identify CLAGN candidates and constructed the follow-up spectroscopic confirmation. About 20% of EVQs were classified as CLAGNs, while the others, though highly variable, did not exhibit broad-line changes large enough to satisfy the disappearance/emergence criterion (MacLeod et al. 2019). This makes EVQs a suitable comparison sample for CLAGNs, under the assumption that the difference arises from the presence or absence of spectral transitions. Using the EVQs from Ren et al. (2022), and since we are interested in accretion- rather than jet-related variability, we cross-match the FIRST survey in radio band (Becker et al. 1995) and rule out 669 radio-detected objects.

For Type 1 AGNs, we start from the SDSS DR 16 Quasar Catalog (Lyke et al. 2020), which contains 750,414 quasars from SDSS I, II, III, and IV. We select the sources with full-width-at-half-maxima (FWHM) of Hβ profile, $\mathrm{FWHM_{H\beta}} > 1500\mathrm{km\,s^{-1}}$.

Type 2 AGNs were selected from the Million Quasar Catalog (MQC) v7.2 (Flesch 2021). We down-selected sources with type/class "K" (narrow-line Seyferts) and/or "N" (narrow-line Quasi-Stellar Objects; QSOs) and crossmatched with the Portsmouth Stellar Kinematics and Emission Line Fluxes Value Added Catalog from SDSS (Thomas et al. 2013). Our final sample consists of 152 CLAGNs, 3690 EVQs, 73963 Type 1 AGNs and 5981 Type 2 AGNs.

We also conduct a control sample of CLAGNs in on/off-state. We select the sources identified in 2015-2023 as CLAGN, and confirm their ZTF lightcurve in a stable phase, using the last spectral classification to distinguish on-state and off-state. Figure 1 shows three examples of cleaned, binned light curves, for the turn-on stable, turn-on unstable and turn-off stable AGNs, respectively. The sources are recently unstable in ZTF light curves are excluded in this control sample. There are 48 off-state light curves and 80 on-state light curves in total.

Given that redshift and black hole mass are less model-dependent in measurement and significantly influence quasar behavior (Hopkins et al. 2007; Kelly et al. 2009), matching these parameters is crucial. For CLAGN, EVQ and Type 1 AGN, the black hole mass, $M_{\rm BH}$, is derived using the single-epoch virial estimators (Vestergaard & Peterson 2006), which rely on the broad emission line width and continuum luminosity as proxies for the virial motion of the broad-line region (BLR). The

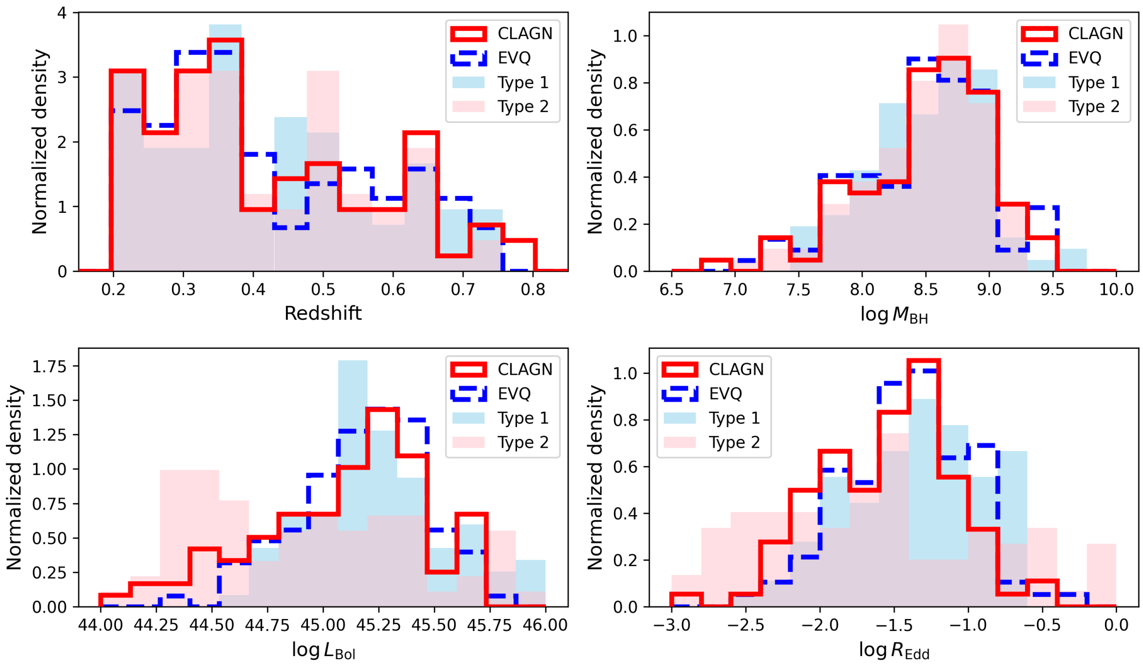

Figure 3. AGN properties for the CLAGN and control samples obtained from the SDSS catalog (Wu & Shen 2022). The skyblue and pink regions refer to Type 1 and Type 2 AGN samples respectively. The blue dashed line represents the distribution of EVQ samples and the red solid line shows the distribution of CLAGN samples.

bolometric luminosity ($L_{\rm bol}$) is estimated based on the continuum luminosity, with a preference for the 3000Å luminosity when available, as it is less affected by host galaxy contamination than the 5100Å luminosity and exhibits lower sensitivity to reddening and variability compared to the 1350Å luminosity (Wu & Shen 2022). The Eddington ratio is computed as $R_{\rm Edd} \equiv L_{\rm bol}/L_{\rm Edd}$, where the Eddington luminosity is given by $L_{\rm Edd} = 1.3 \times 10^{38} \left(\frac{M_{\rm BH}}{M_\odot}\right) \,{\rm erg\,s^{-1}}$. For EVQ and Type 1 AGN, these quantities are adopted from Wu & Shen (2022).

The black hole mass of Type 2 AGN is estimated using the M–σ relation from Ferrarese (2002):

$$M_{\rm BH} = (1.66 \pm 0.32) \times 10^8 M_\odot \left(\frac{\sigma_*}{200 \text{ km s}^{-1}}\right)^{4.58\pm0.52}, \tag{1}$$

where the stellar velocity dispersion σ_* is taken from the Portsmouth group galaxy properties catalog (Thomas et al. 2013).

We adopt the extinction-corrected [O III] λ5007 line fluxes from the Portsmouth catalog (Thomas et al. 2013), which are corrected for the diffuse dust component affecting the overall spectral shape by using the Calzetti (2001) obscuration curve and not including Balmer-decrement based dust corrections. We then use them to estimate the bolometric luminosity, $L_{\rm bol}$, following Pennell et al. (2017), as

$$L_{[\rm O\,III]} = 4\pi D_L^2 F_{[\rm O\,III]}, \tag{2}$$

$$\log\left(\frac{\rm L_{bol}}{\rm erg\ s^{-1}}\right) = \log\left(\frac{\rm L_{[O\,III]}}{\rm erg\ s^{-1}}\right) + (3.532 \pm 0.059), \tag{3}$$

where D_L is the luminosity distance derived from the redshift.

We note that this approach is subject to systematic uncertainties, including the intrinsic scatter in the M–σ relation and the potential contamination of [O III] luminosity by star formation or shock excitation.

To construct a control sample of EVQs, Type 1 AGNs, and Type 2 AGNs that matches the CLAGNs in both black hole mass and redshift, we adopt a two-dimensional probability matching scheme, which statistically reproduces the distributions of CLAGNs in z and $M_{\rm BH}$. To maintain consistency across samples, we restricted all sources to $z > 0.2$, as the EVQ sample contains very few objects at redshifts lower than 0.2. After this cut, 90 CLAGNs remained in our sample. Specifically, the black hole mass range is $10^{6.5}$ to $10^{10} M_\odot$ and is divided into 10 logarithmic bins, while the redshift range is $0.2 < z < 0.8$ and is divided into 10 uniform bins for the probability matching. The left and middle panels of Figure 2 show the 2D distributions of CLAGNs and Type 2 AGNs in the $(\log M_{\rm BH}, z)$ plane, while the right panel presents the logarithmic ratio between the two. Each object in the control sample was assigned a weight proportional to the ratio of these densities, and 90 sources were randomly drawn using the normalized weights as selection probabilities. As seen in the figure, the Type 2 AGN sample has fewer sources in the four corners of the 2D parameter space, which leads to higher statistical uncertainty when sampling control sources from these regions. As a result, even though the matching procedure is probabilistic, the reconstructed control sample may show larger fluctuations at the distribution edges, particularly where the original Type 2 density is low. This illustrates a limitation of the matching method in regions where the control sample has intrinsically sparse coverage. In our analysis, we also conducted a comparison without controlling for redshift and black hole mass, by drawing random subsamples of equal size from the full control sets, and the results did not show significant differences.

To ensure fair comparisons, we adopted a 1:1:1:1 matching scheme so that the scatter in their distributions is comparable. After applying the matching, we obtained final samples of 90 CLAGNs, 90 EVQs, 90 Type 1 AGNs, and 90 Type 2 AGNs. The resulting control samples exhibit $M_{\rm BH}$ and z distributions statistically consistent with those of the CLAGNs, as confirmed by the Kolmogorov-Smirnov (KS) test. Figure 3 shows the normalized density of bolometric luminosity, $L_{\rm bol}$ and Eddington ratio, $R_{\rm Edd}$. Values of $L_{\rm bol}$ and $R_{\rm Edd}$ are adopted from Wu & Shen (2022) when available, so the distribution shown is mostly for the bright-state spectra. For the sources in Yang et al. (2025), both dim- and bright-state measurements are available, and we adopt the bright-state values to remain consistent with Wu & Shen (2022).

3. RESULTS

3.1. *Color variability*

Previous studies have shown that CLAGNs generally follow the well-known "bluer-when-brighter" trend in the optical bands, similar to normal Type 1 AGNs (Yang et al. 2018). To investigate this in more detail, we analyzed the color variability of CLAGNs using ZTF light curves in the g- and r- bands. The light curves were binned in 3-day intervals, and for epochs with observations in both bands, we computed the $g-r$ (hereafter we denote g and r as the ZTF $zg-$ and zr-band) color and the change in zg-band magnitude, Δg. Here, a negative Δg indicates that the object becomes brighter, and a negative color variability value corresponds to a bluer color.

Using this dataset, we constructed the color-magnitude diagrams ($zg - zr$ vs. zg) for each CLAGN, with representative examples SDSS J0040+1609 shown in Figure 4. To quantify the color variability, we fit the color-magnitude relation with a linear function:

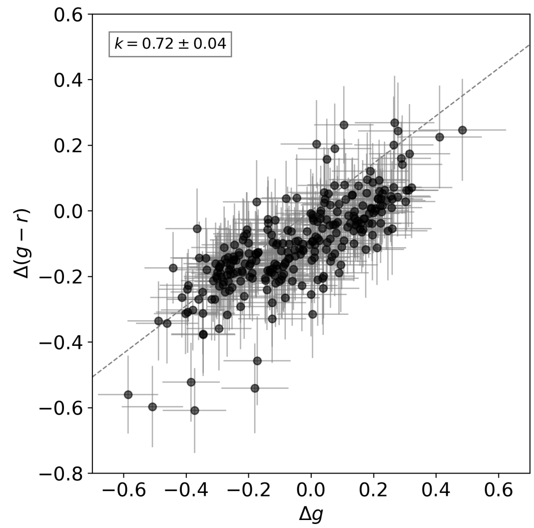

Figure 4. Color variability vs. magnitude variability for the CLAGN, SDSS J0040+1609, in the optical band. The gray dashed line represents the best-fit linear relation. The data confirm a bluer-when-brighter trend.

$$\Delta(g - r) = k \times \Delta g, \quad (4)$$

where k represents the slope of the relation. A positive k value indicates a "bluer-when-brighter" trend, while a negative k value corresponds to the "redder-when-brighter" pattern.

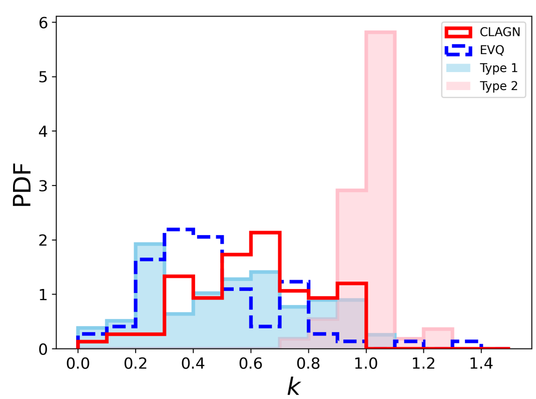

Figure 5. Distributions of the k values (slopes) from the linear fits to the color-magnitude variation data points for CLAGNs and the corresponding control samples. The lines have the same meaning as in Figure 1. Type 1 AGN and Type 2 AGN share different distribution while CLAGN located in the middle region.

To ensure the reliability of the k values, we computed the Pearson correlation coefficient during the fitting procedure and excluded sources with a correlation significance level of $p > 0.05$. Figure 5 displays the distribution of k values for CLAGNs and their corresponding control samples. Type 1 AGNs exhibit a central k value around 0.50, consistent with the typical variability behavior of unobscured AGNs. Type 2 AGNs, in contrast, show a steeper slope, with k values centered around 1.0. The distribution of EVQs is similar to Type 1 AGNs, while CLAGNs occupy an intermediate region between Type 1 and Type 2 AGNs. This suggests that CLAGNs exhibit color variability properties distinct from both normal Type 1 and Type 2 AGNs, potentially reflecting their transitional nature.

We illustrate the differences in color variability among different samples and summarize the mean and standard deviation of the color variability slopes, k, in Table 3. The values confirm the observed trend in Figure 5, with Type 1 AGNs showing the smallest slopes and Type 2 AGNs exhibiting the steepest changes. EVQs show little difference with Type 1 AGNs while CLAGNs fall in between, further supporting the intermediate nature.

To further investigate the behavior of CLAGNs in different spectral states, we separately analyzed the color-magnitude slopes for the on-state and off-state epochs (Figure 6). Notably, the k distribution for the off-state CLAGNs does not align with that of normal Type 2 AGNs, and similarly, the on-state distribution differs from that of normal Type 1 AGNs. To further quantify the similarity between the color variability slopes of on-state / off-state CLAGNs and those of the control samples, we performed KS tests on these samples. Table 4 represents the KS statistics and p-values for different comparisons.

The KS test results indicate that both on- and off-state CLAGNs are generally more similar to the overall CLAGN sample than to their respective control AGN types. Specifically, on-state CLAGNs are closer to the overall CLAGN distribution than to Type 1 AGNs ($p = 0.631$ vs. $p = 0.363$), and off-state CLAGNs are closer to the overall CLAGN distribution than to Type 2 AGNs ($p = 0.848$ vs. $p = 6.96 \times 10^{-18}$). These findings support the idea that CLAGN variability is not simply a direct transition between Type 1 and Type 2, thus the variability properties of CLAGNs are not simply a combination of distinct Type 1 and Type 2 behaviors, but represent an intermediate mode.

3.2. *Structure Function (SF)*

The structure function (SF) is a widely used statistical tool for characterizing the variability of AGNs by quantifying how the amplitude of variability depends on the time separation between observations. For objects with $n_{\Delta t}$ light curve data points, the observed variability amplitude between epochs with separation Δt is (Kozłowski 2016),

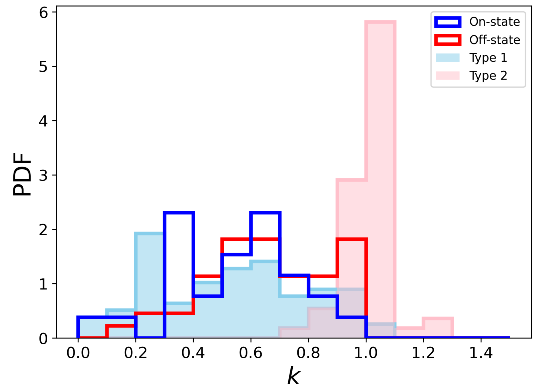

Figure 6. Distributions of the k values (slopes) from the linear fits to the color-magnitude variation data points for on/off-state and the corresponding control sample. The sky-blue and pink lines represent Type 1 and Type 2 AGNs. The blue and red lines show the on-state and off-state sources, which have a similar distribution located in the middle region.

$$SF_{ij,obs} = \sqrt{\frac{1}{n_{\Delta t}} \sum_{i,j} \left\{ [m_i - m_j]^2 - \sigma_i^2 - \sigma_j^2 \right\}}. \quad (5)$$

Here, the summation is taken over all epoch pairs i, j with time separations that fall within a given time lag bin Δt in the rest frame. The measured magnitudes at epochs i and j are denoted by m_i and m_j, and their respective photometric uncertainties are σ_i and σ_j with a 0.9 factor (Kim et al. 2024).

This structure function can be described with a power-law model (Schmidt et al. 2010):

$$SF_{ij,\text{ model}} = A \left(\frac{|t_i - t_j|}{1\text{yr}} \right)^{\gamma}, \quad (6)$$

where A refer to the typical variability for 1 year, and γ is the logarithmic gradient of this mean change in magnitude.

We use a simple Markov chain Monte Carlo (MCMC) approach to estimate the parameters A and γ. The likelihood function is given by:

$$\mathcal{L}(A, \gamma) = \prod_{i,j} L_{i,j}, \quad (7)$$

assuming the magnitude difference in CLAGN is independent. The $L_{i,j}$ is the likelihood of observing magnitude difference $\Delta m_{i,j}$ between two light curve points separated by $\Delta t_{i,j}$ for a single source.

We assume an underlying Gaussian distribution of Δm values and Gaussian photometric errors, then the

Table 3. Mean and standard deviation of color variability slopes, k, and variability metrics for different samples (updated).

Sample	k	$\log(1+\sigma_{\rm QSO})$	$\log(1+\sigma_{\rm var})$	$f(\sigma_{\rm QSO}>3)$
CLAGN	0.61 ± 0.21	1.025 ± 0.324	1.440 ± 0.429	0.873
On-state	0.55 ± 0.22	1.063 ± 0.282	1.568 ± 0.383	0.926
Off-state	0.65 ± 0.21	0.987 ± 0.344	1.419 ± 0.454	0.830
EVQ	0.46 ± 0.24	1.031 ± 0.351	1.673 ± 0.493	0.881
Type 1 AGN	0.53 ± 0.27	0.923 ± 0.352	1.421 ± 0.500	0.874
Type 2 AGN	1.02 ± 0.08	0.281 ± 0.137	0.579 ± 0.280	0.169

Table 4. Kolmogorov-Smirnov test results for the on/off-state CLAGNs and control samples (updated)

Comparison	D_k	p_k	$D_{\log(1+\sigma_{\rm QSO})}$	$p_{\log(1+\sigma_{\rm QSO})}$	$D_{\log(1+\sigma_{\rm var})}$	$p_{\log(1+\sigma_{\rm var})}$
On-State vs. Type 1	0.2051	3.63×10^{-1}	0.2095	2.80×10^{-1}	0.2312	1.86×10^{-1}
Off-State vs. Type 2	0.8364	6.96×10^{-18}	0.7080	9.70×10^{-14}	0.6890	5.75×10^{-13}
On-State vs. CLAGN	0.1610	6.31×10^{-1}	0.1303	8.31×10^{-1}	0.1430	7.42×10^{-1}
Off-State vs. CLAGN	0.1094	8.48×10^{-1}	0.1045	8.60×10^{-1}	0.1131	7.92×10^{-1}
On-State vs. EVQ	0.3590	9.84×10^{-3}	0.2183	2.43×10^{-1}	0.2222	2.25×10^{-1}
Off-State vs. EVQ	0.4848	1.86×10^{-6}	0.2302	6.72×10^{-2}	0.2191	9.21×10^{-2}

likelihood can be defined as

$$L_{i,j}=\prod_{i,j}\frac{1}{\sqrt{2\pi\sigma^2_{SF,ij}}}\times\exp\left(-\frac{\left(SF_{ij}-SF_{ij,\text{ model }}\right)^2}{2\sigma^2_{SF,ij}}\right). \quad (8)$$

The uncertainty in the structure function, $\sigma_{SF,ij}$, was estimated using a bootstrap resampling method. For each time bin, we randomly selected 80% of the available data points, recalculated SF_{ij} 1000 times, and took the standard deviation of these realizations as $\sigma_{SF,ij}$.

For the prior distributions, we adopted an uninformative log-uniform prior for A, $P(A)\propto 1/A$ with $A\in(0,1)$, and an arctangent-uniform prior for γ, $P(\gamma)\propto 1/(1+\gamma^2)$, $\gamma\in(0,+\infty)$ (Schmidt et al. 2010).

To ensure the robust estimates, we used logarithmic binning in the time domain to balance the number of data points in each bin. We cut out the vibration tail for each source(Tang et al. 2023). For each light curve, the cut fraction was determined by scanning within the 0.2–0.8 range and selecting the fraction that yields the best linear fit of the structure function. Sources with fewer than 20 data points remaining after this cut were excluded. The parameters A and γ were then estimated for the remaining CLAGNs and control sample objects.

There are 71 CLAGNs, 66 EVQs, 75 Type 1s, and 38 Type 2s considered in this section. Most of the excluded sources are Type 2s at slightly higher redshifts, but the overall redshift and black hole mass distributions are not significantly affected, and thus the impact on our results is negligible. Figure 7 illustrates the procedure for an example of a CLAGN.

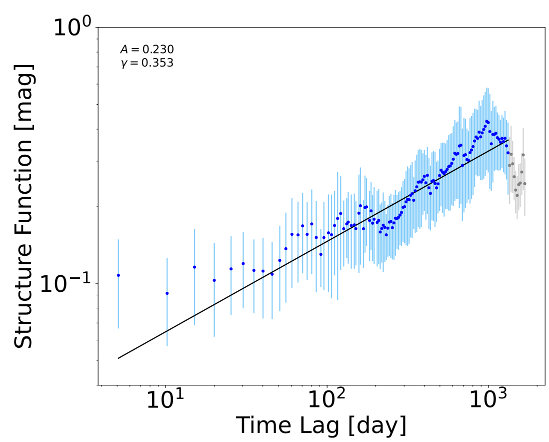

Figure 7. Structure function of a CLAGN SDSS J0040+1609. The points represent the observed SF, while the black line shows the best-fit power-law model, characterized by the estimated parameters A and γ. The gray points were cut off to avoid the noisy vibration tail at longer time lags.

Figure 8 presents the distribution of the variability characteristics, quantified by the best-fit A and γ for the selected sources with zg band data. The histograms along the axes of the two-dimensional scatter plot show the parameter projected distribution of the CLAGNs and control samples. Notably, our results, particularly the A–γ distribution of the Type 1 AGNs, are broadly consistent with those of QSOs reported by Schmidt et al.

(2010), although our parameter range appears narrower, likely due to the smaller sample size.

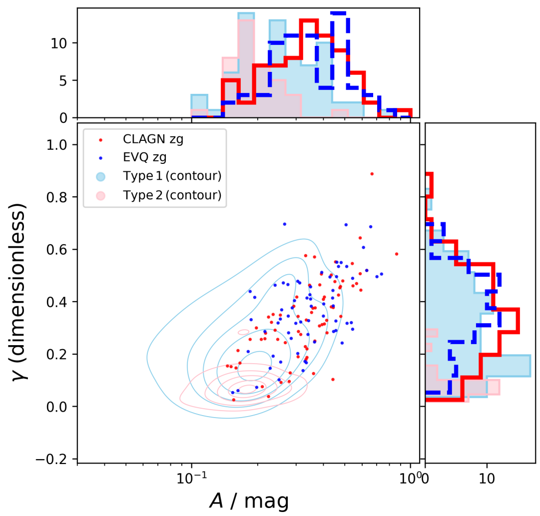

Figure 8. Comparison of A and γ for different AGN samples: CLAGN in red points, EVQ in blue points, Type 1 AGNs in skyblue contour, and Type 2 AGNs in pink contour. The top and right panel show the histogram for A and γ. The scatter plot highlights distinct clustering: CLAGNs and EVQs generally exhibit larger A values compared to Type 1 AGNs and Type 2 AGNs, indicating greater variability. EVQs and Type 1 AGNs tend to have higher γ than CLAGN, while Type 2 AGNs are concentrated at even lower values. This demonstrates significant differences in variability properties across AGN types.

Overall, these results highlight that CLAGNs exhibit stronger and more rapidly evolving variability compared to typical Type 2 AGNs, with a distribution of SF parameters more similar to EVQs and Type 1 AGNs. The distinction in the structure function properties between CLAGNs and other AGN types provides further insight into their unique variability behavior.

3.3. *Variability metric*

Type 1 and Type 2 AGNs exhibit distinct variability properties due to differences in their accretion physics and dust obscuration. While Type 1 AGNs show strong, stochastic variability, primarily driven by fluctuations in the accretion disk, Type 2 AGNs exhibit significantly weaker variability, likely due to the presence of a dusty torus that obscures the variable continuum (Kovacevic et al. 2025). Since CLAGNs experience transition between these two types, it is crucial to investigate whether their variability characteristics also evolve during different phases of the transition, as this can provide insight into the underlying physical mechanisms governing CLAGN behavior.

In this section, we quantify the variability statistics using the qso_fit software[2] (Butler & Bloom 2011), which was developed to separate (type 1) quasars from other point-like sources (e.g., stars) in SDSS Stripe 82 based on their g band light curves.

We adopt two parameters in the variability metric to describe the variability. (i) $\sigma_{\rm var}$ assesses whether the source is variable, and the significance of variability; (ii) $\sigma_{\rm QSO}$ quantifies the source variability prefer to be described by a DRW model rather than a time-independent variable Gaussian signals. The details and definition are presented in Appendix A. Combined, these metrics have been proven to efficiently separate quasars from stars with high completeness (>99%) and low contamination (<3%) in SDSS Stripe 82 (Butler & Bloom 2011). In particular, $\sigma_{\rm QSO} > 3$ has been used to be a indicator of quasar-like variability, and thus serves as an effective selection threshold. Accordingly, in addition to computing both variability metric parameters, we also evaluate the fraction of sources with $\sigma_{\rm QSO} > 3$, $f(\sigma_{\rm QSO} > 3)$, in each sample for further comparison.

As shown in Figure 9, Type 1 and Type 2 AGNs exhibit well-separated distributions in both $\sigma_{\rm QSO}$ and $\sigma_{\rm var}$. Type 1 AGNs display high values of both parameters, reflecting their strong and DRW-like variability, which is characteristic of accretion disk fluctuations. In contrast, Type 2 AGNs have lower values of $\sigma_{\rm QSO}$ and $\sigma_{\rm var}$, indicating significantly weaker variability, likely due to the obscuration of the accretion disk by the dusty torus.

Rather than exhibiting a bimodal or double-peak distribution, CLAGNs and EVQs occupy a continuous distribution centered between Type 1 and Type 2 AGNs, or more close to Type 1 AGNs. Meanwhile, their $f(\sigma_{\rm QSO} > 3)$ values are more close to Type 1 AGNs.

Similar to the color-magnitude relation, we compare the distributions of on-state and off-state CLAGNs with those of Type 1 and Type 2 AGNs in the $\log(1 + \sigma_{\rm QSO})$ vs. $\log(1 + \sigma_{\rm var})$ plane (g band) in Figure 10. Notably, for $\sigma_{\rm QSO}$, the on-state CLAGNs do not exhibit a strong resemblance to typical Type 1 AGNs, nor do the off-state CLAGNs show a clear similarity to Type 2 AGNs. Instead, both states tend to occupy regions closer to the overall CLAGN distribution, suggesting that the variability properties of CLAGNs are not simply a superposition of Type 1 and Type 2 characteristics, but reflect an intrinsically distinct variability behavior. For $\sigma_{\rm var}$, the variability in the off-state sample is smaller than that in the on-state sample, but still larger than that of Type 2 AGNs. We also list the corresponding variability

[2] https://github.com/wt-liao/quasar_drw

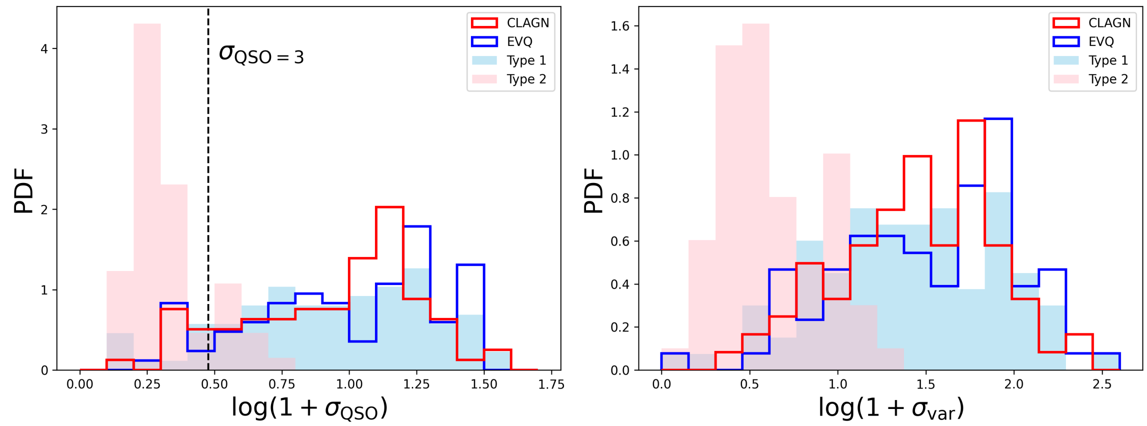

Figure 9. Comparison of $\sigma_{\rm QSO}$ and $\sigma_{\rm var}$ for different AGN samples: CLAGN in red line, EVQ in blue line, Type 1 AGNs in skyblue region, and Type 2 AGNs in pink region. The majority of Type 1 and 2 AGNs are well separated while CLAGNs and EVQs locate in the middle region.

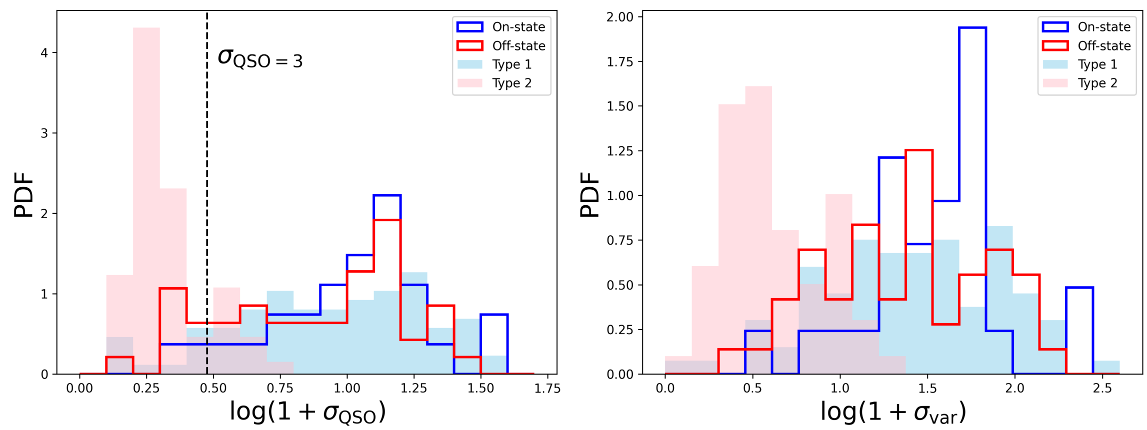

Figure 10. Comparison of $\sigma_{\rm QSO}$ and $\sigma_{\rm var}$ for different AGN samples: off-state in red line, on-state in blue line, Type 1 AGNs in skyblue region, and Type 2 AGNs in pink region. Both on-state and off-state CLAGNs locate in the middle region.

metric result of each sample in Table 3, in which Type 2 AGNs exhibit significantly lower values, while the differences among the other samples remain relatively small.

We also performed KS tests on the distributions of variability metrics, and the results are shown in Table 4. The KS statistics indicate that both the on-state and off-state CLAGNs differ substantially from the Type 1 and Type 2 AGN control samples, respectively. In contrast, the KS statistics are much smaller when comparing the on-/off-state CLAGNs with the overall CLAGNs, consistent with the similarities described above. These results quantitatively support our conclusions and are in agreement with the trends indicated by the higher fraction of sources with $\sigma_{\rm QSO} > 3$.

Physically, this behavior is consistent with the scenario in which CLAGNs experience significant changes in their accretion states (Ricci & Trakhtenbrot 2023). The increase in variability compared to Type 2 AGNs suggests that at least part of the accretion disk becomes directly observable during the state transitions. Meanwhile, the similarity between CLAGNs and EVQs in their variability distributions implies that the same underlying mechanisms.

4. DISCUSSION

4.1. *Variability - Type Transition?*

Although the physical mechanisms driving CLAGNs remain unclear, variability studies play a crucial role in probing the physics of the central regions of AGNs. In particular, variability provides key constraints on accretion disk instabilities, the structure and reprocessing effects of the broad-line region (BLR), and the role of dust obscuration. Unlike the static spectral classification, variability-based studies offer a dynamic perspective on AGN evolution, making them essential for understanding the nature of CLAGNs.

As shown in Table 1, many previous searches for CLAGNs have focused on cases exhibiting extreme photometric variability. For these studies, the success rate of follow-up spectroscopic confirmation is highly dependent on the arbitrarily chosen variability threshold and the signal-to-noise ratio (SNR) of the observations, which remains moderate, typically around 15–50% (Yang et al. 2018; MacLeod et al. 2019). While these selection methods have identified a number of CLAGNs, they may also introduce biases, potentially missing sources that undergo transitions in short timescales due to the time gaps between different surveys. The cadence and depth of photometric surveys also play a crucial role in detection efficiency, as shorter-duration surveys may fail to capture the full variability cycle of some CLAGNs.

In addition to photometric selection, some studies have employed variability-based methods to search for CLAGNs. Zhu et al. (2025) utilized a color-magnitude pattern as a selection criterion, achieving a success rate of approximately 45%, comparable to the traditional photometric variability methods. Wang et al. (2024) adopted a variability metric approach, yielding a higher success rate of around 80%, demonstrating greater efficiency than the photometric methods. These studies generally assume that Type 1 and Type 2 AGNs exhibit distinct variability patterns, and classify CLAGNs by comparing their current variability properties to former spectral types. Implicitly, these methods rely on the assumption that the variability characteristics of CLAGNs are tied to their spectral classifications.

Our study specifically investigates the variability properties of CLAGNs and challenges the assumption that their variability mode is inherently tied to spectral classification. We find that variability-based transitions do not always correspond to spectral state transitions, suggesting that these two processes may be independent rather than intrinsically linked.

Traditionally, CLAGNs are defined by the appearance or disappearance of broad emission lines—a classification based on spectral features rather than a quantitative measure of variability. This definition implies a clear transition between a bright state and a dim state, each associated with a distinct AGN type. However, our analysis reveals that the variability properties of CLAGNs remain largely consistent across these spectral states. Additionally, CLAGNs exhibit variability characteristics that systematically differ from both Type 1 and Type 2 AGNs, challenging the notion that they undergo a complete and discrete type transition.

In our study, we found that CLAGNs exhibit an intermediate variability mode compared to Type 1 and Type 2 AGNs. A systematic comparison between on-state and off-state sources did not reveal significant differences, suggesting that the variability mode remains unchanged despite the observed spectral type transition. This result is consistent with Jana et al. (2025), who compared the variability properties of CLAGNs and normal AGNs of different types (see their Figure 4). The existence of this intermediate variability mode raises important questions about the physical nature of CLAGNs—whether they undergo genuine transitions between Type 1 and Type 2 states or instead continuously occupy a critical regime between the two, with spectral transitions occurring as a result of moderate fluctuations in accretion rate. In this scenario, CLAGNs do not fully switch between distinct AGN types but rather oscillate within a transitional state, where changes in accretion conditions temporarily enhance or suppress broad-line emission. Further investigation into the variability timescales and Eddington ratio evolution of CLAGNs will be essential to distinguish between these possibilities and to establish whether accretion rate fluctuations alone can account for their observed spectral changes.

4.2. *Naked Type 2 AGN?*

The term naked Type 2 AGNs was first introduced to describe AGNs that lack both a broad-line region (BLR) and significant obscuration in the X-ray or optical bands (Hawkins 2004; Panessa et al. 2009). Unlike traditional Type 2 AGNs, where the absence of broad emission lines is attributed to dust obscuration, naked Type 2 AGNs are thought to be intrinsically lacking a BLR, possibly due to a low accretion rate or a different accretion disk structure (LaMassa et al. 2014). Theoretical models suggest that at sufficiently low Eddington ratios ($R_{\rm Edd} \lesssim 0.01$), the accretion flow may become radiatively inefficient, suppressing the formation of a standard BLR(Noda & Done 2018; Ricci & Trakhtenbrot 2023).

The nature of CLAGNs suggests a possible link to naked Type 2 AGNs. Since CLAGNs are once believed to exhibit transitions between Type 1 and Type 2 states, one scenario is that they represent AGNs fluctuating near the critical threshold where the BLR becomes unstable or disappears altogether. If CLAGNs in their Type 2 phase are intrinsically lacking a photoionized BLR rather than being obscured, they may effectively be transient naked Type 2 AGNs. This interpretation is supported by the fact that some CLAGNs remain in a Type 2 state without showing signs of heavy obscuration (Yang et al. 2023; Jana et al. 2025). In this case, CLAGNs could provide a valuable population for studying the physics of the BLR and its dependence on accretion rate.

Furthermore, if CLAGNs contain a significant fraction of naked Type 2 AGNs, they serve as ideal candidates for investigating variability in low-Eddington ratio AGNs, particularly in the X-ray regime. X-ray variability is a key diagnostic of accretion processes in AGNs, and in low-$\lambda_{\rm Edd}$ systems, changes in the spectral index ($\alpha_{\rm OX}$) have been shown to correlate with the Eddington ratio (Yang et al. 2023; Hagen et al. 2024). Systematically, when $R_{\rm Edd} \gtrsim 0.01$, AGNs tend to exhibit harder X-ray spectra (lower $\alpha_{\rm OX}$) when $R_{\rm Edd}$ decrease. By contrast, when $R_{\rm Edd} \lesssim 0.01$, $\alpha_{\rm OX}$ soften when $R_{\rm Edd}$ getting smaller, consistent with a transition to a radiatively inefficient accretion flow (Yang et al. 2023).

Tracking these trends across individual AGNs at different accretion rates, especially at the low-$R_{\rm Edd}$ end, is crucial for understanding accretion physics. However, variability studies of normal low-$R_{\rm Edd}$ AGNs are challenging, as they are often heavily obscured Type 2 AGNs, where intrinsic variability is significantly suppressed or entirely hidden. In contrast, CLAGNs, particularly those in their off-state, may provide a unique opportunity to probe accretion physics at low-$R_{\rm Edd}$ with less obscuration.

If CLAGNs in their off-state resemble low-$R_{\rm Edd}$ AGNs, their X-ray spectral variability can provide insight into the accretion physics at play (Noda & Done 2018; Lyu et al. 2025). Future studies combining X-ray data (e.g., from Chandra and XMM-Newton) and optical spectroscopic monitoring could test whether CLAGNs follow the same $\alpha_{\rm OX}$–$R_{\rm Edd}$ relation as other low-luminosity AGNs, further implying their nature.

5. CONCLUSION

We constructed a sample of 152 CLAGNs from the literature, all exhibiting clear spectral transitions characterized by the appearance or disappearance of broad emission lines. To enable a meaningful comparison, we established a control sample consisting of EVQs, Type 1 AGNs, and Type 2 AGNs, matched in redshift and SMBH mass. This control sample allows us to investigate potential differences in variability behavior across various AGN populations.

We further divided the CLAGNs into turn-on and turn-off subsamples based on their most recent spectral classifications. This categorization enables a direct comparison between spectral transitions and corresponding photometric variability.

A bluer-when-brighter trend is confirmed for CLAGNs in the optical bands, as shown in their color–magnitude relation. CLAGNs occupy an intermediate region between Type 1 and Type 2 AGNs in this color–magnitude space. Despite their evident spectral transitions between on-state and off-state phases, we do not observe significant differences in their color–magnitude trends across these states.

In terms of structure function analysis, both CLAGNs and EVQs show systematically larger A values than Type 1 and Type 2 AGNs, indicating stronger variability amplitudes. CLAGNs exhibit lower γ values compared to EVQs and Type 1 AGNs, while Type 2 AGNs cluster at even lower γ.

We also investigated the variability metrics $\sigma_{\rm QSO}$ and $\sigma_{\rm var}$ across all samples. While most Type 1 AGNs show high values in both metrics and Type 2 AGNs cluster at low values, CLAGNs and EVQs display a continuous distribution centered in a critical regime between the two types. Notably, on-state CLAGNs do not strongly resemble typical Type 1 AGNs, nor do off-state CLAGNs align with Type 2 AGNs. Instead, both phases of CLAGNs share similar variability properties with each other, further supporting the idea that CLAGNs occupy a distinct and transitional variability regime.

Taken together, these results suggest that the variability pattern of CLAGNs does not fundamentally change with their spectral state. Rather than representing simple switches between classical Type 1 and Type 2 AGN modes, CLAGNs are more likely to represent a special, critical state of AGN activity.

We thank the anonymous referee for a very constructive report which significantly helps us to revise the paper. We thank the support of the National Key R&D Program of China (grant No. 2022YFF0503401) and the National Science Foundation of China (grant No. 12133001). This work is based on observations obtained with the Samuel Oschin Telescope 48 inch and the 60 inch Telescope at the Palomar Observatory as part of the Zwicky Transient Facility project. ZTF is supported by the National Science Foundation under grant No. AST-2034437 and a collaboration including Caltech, IPAC, the Weizmann Institute for Science, the Oskar Klein Center at Stockholm University, the University of Maryland, Deutsches Elektronen-Synchrotron and Humboldt University, the TANGO Consortium of Taiwan, the University of Wisconsin at Milwaukee, Trinity College Dublin, Lawrence Livermore National Laboratories, and IN2P3, France. Operations are conducted by COO, IPAC, and UW.

Funding for the Sloan Digital Sky Survey IV has been provided by the Alfred P. Sloan Foundation, the U.S. Department of Energy Office of Science, and the Participating Institutions.

SDSS-IV acknowledges support and resources from the Center for High Performance Computing at the University of Utah. The SDSS website is www.sdss4.org.

SDSS-IV is managed by the Astrophysical Research Consortium for the Participating Institutions of the SDSS Collaboration including the Brazilian Participation Group, the Carnegie Institution for Science, Carnegie Mellon University, Center for Astrophysics — Harvard & Smithsonian, the Chilean Participation Group, the French Participation Group, Instituto de Astrofísica de Canarias, The Johns Hopkins University, Kavli Institute for the Physics and Mathematics of the Universe (IPMU) / University of Tokyo, the Korean Participation Group, Lawrence Berkeley National Laboratory, Leibniz Institut für Astrophysik Potsdam (AIP), Max-Planck-Institut für Astronomie (MPIA Heidelberg), Max-Planck-Institut für Astrophysik (MPA Garching), Max-Planck-Institut für Extraterrestrische Physik (MPE), National Astronomical Observatories of China, New Mexico State University, New York University, University of Notre Dame, Observatário Nacional / MCTI, The Ohio State University, Pennsylvania State University, Shanghai Astronomical Observatory, United Kingdom Participation Group, Universidad Nacional Autónoma de México, University of Arizona, University of Colorado Boulder, University of Oxford, University of Portsmouth, University of Utah, University of Virginia, University of Washington, University of Wisconsin, Vanderbilt University, and Yale University.

APPENDIX

A. DEFINITION OF VARIABILITY METRIC

We adopt two significance measures to assess the quasar-like variability in light curves, following the damped random walk (DRW) formalism described by Butler & Bloom (2011).

For objects with n light curve data points, the number of degrees of freedom $\nu = n-1$. Let the measured magnitudes at two epochs i and j are m_i and m_j, their respective photometric uncertainties are σ_i and σ_j, and the error-weights are, $w_i = 1/\sigma_i^2$. From Butler & Bloom (2011), the exponential damping timescale have, $\log(\tau_\circ) = 2.92-0.07\times(m-19)$, and the intrinsic variance between observations on short timescales $\tau_{ij} \sim 1$ days, $\log(\hat{\sigma}^2) = -4.1 + 0.14 \times (m-19)$.

Supposed that the quasar variability as a function of time difference is modeled using a covariance matrix of the form:

$$C_{ij} = \sigma_i^2\delta_{ij} + \frac{1}{2}\hat{\sigma}^2\tau_\circ \exp\left(-\tau_{ij}/\tau_\circ\right) \tag{A1}$$

where δ_{ij} is the Kronecker delta function (1 for $i = j$, 0 otherwise)

Then we have,

$$\chi^2_{\rm QSO} = \left(x - x_{\circ,\rm best}\right)^T C^{-1}\left(x - x_{\circ,\rm best}\right), \tag{A2}$$

in which, $x_{\circ,\text{ best}} = \sum_{i,j} C_{ij}^{-1} x_j / \sum_{i,j} C_{ij}^{-1}$.

The first metric, $\sigma_{\rm QSO}$, quantifies how significantly the observed variability resembles a quasar-like DRW model compared to a generic variable source. It is derived from the probability $p_{\rm QSO}$ that the reduced chi-squared value of the DRW fit, $\chi^2_{\rm QSO}/\nu$, is lower than that expected for a non-quasar variable.

This probability is computed using the regularized incomplete beta function. Firstly, the ratio x can be written as:

$$x = \frac{\chi^2_{\rm QSO}}{\chi^2_{\rm QSO} + {\rm Tr}(C^{-1})\cdot v_m}, \text{in which } v_m = \langle m^2\rangle - \langle m\rangle^2, \tag{A3}$$

then the probability could be calculated by the regularized incomplete beta function:

$$p_{\rm QSO} = I_x\left(\frac{\nu}{2}, \frac{\nu}{2}\right), \tag{A4}$$

and the final significance is converted into Gaussian sigma units:

$$\sigma_{\rm QSO} = \Phi^{-1}\left(1 - \frac{1}{2}p_{\rm QSO}\right), \tag{A5}$$

where Φ^{-1} is the inverse cumulative distribution function of the standard normal distribution.

The second metric, $\sigma_{\rm var}$, evaluates how strongly the light curve deviates from a constant-flux (non-variable) model. It is based on the classical reduced chi-squared value $\chi^2_{\rm var}/\nu$, and the corresponding upper-tail probability $p_{\rm vary}$,

From the total chi-squared:

$$x = \chi^2_{\rm var} = \sum_{i=1}^{n} \frac{\left(m_i - \bar{m}_w\right)^2}{\sigma_i^2}, \text{in which } \bar{m}_w = \frac{\sum_{i=1}^n w_i m_i}{\sum_{i=1}^n w_i}, \tag{A6}$$

and the probability is described by the regularized upper incomplete gamma function:

$$p_{\rm vary} = Q\left(\frac{\nu}{2}, \frac{x}{2}\right), \tag{A7}$$

and the final metric $\sigma_{\rm var}$ is computed from the regularized incomplete gamma function:

$$\sigma_{\rm var} = \Phi^{-1}\left(1 - \frac{1}{2}p_{\rm vary}\right). \tag{A8}$$

Both metrics are expressed in units of Gaussian sigma, where higher values indicate stronger statistical significance.

Table 5. Summary of CLAGN Sources

Reference	Name	Coordinate	Redshift	Phase
MacLeod et al. (2016)	J0159+0033	01:59:57.64+00:33:10.50	0.31204	off
	J0023+0035	00:23:11.06+00:35:17.53	0.422105	on
	J0225+0030	02:25:56.08+00:30:26.72	0.503908	on-off
	J0226-0039	02:26:52.24-00:39:16.50	0.625329	off
	J1002+4509	10:02:20.19+45:09:27.30	0.400894	off
	J1021+4645	10:21:52.35+46:45:15.71	0.20413	off
	J1324+4802	13:24:57.30+48:02:41.32	0.27156	off
	J2146+0009	21:46:13.31+00:09:30.79	0.622	on
	J2252+0109	22:52:40.37+01:09:58.71	0.533515	on
	J2333-0023	23:33:17.39-00:23:03.53	0.51301	on
Yang et al. (2018)	J0831+3646	08:31:32.25+36:46:17.27	0.19501	on
	J0849+2747	08:49:57.79+27:47:28.96	0.29854	off
	J0909+4747	09:09:32.02+47:47:30.69	0.11694	on
	J0937+2602	09:37:30.33+26:02:32.14	0.16219	on
	J1003+3525	10:03:23.46+35:25:03.84	0.11886	on
	J1104+6343	11:04:23.21+63:43:05.36	0.16427	off
	J1104+0118	11:04:55.17+01:18:56.64	0.57514	off
	J1110-0003	11:10:25.45-00:03:34.14	0.21922	on
	J1115+0544	11:15:36.57+05:44:49.73	0.08995	on
	J1118+3203	11:18:29.64+32:04:00.00	0.3651	off
	J1132+0357	11:32:29.14+03:57:29.08	0.09089	on
	J1150+3632	11:50:39.32+36:32:58.43	0.34004	off
	J1152+3209	11:52:27.49+32:09:59.45	0.37432	off
	J1259+5515	12:59:16.74+55:15:07.15	0.19865	on
	J1319+6753	13:19:30.74+67:53:55.37	0.16643	on
	J1358+4934	13:58:55.83+49:34:14.11	0.11592	on
	J1447+2833	14:47:54.24+28:33:24.10	0.16344	on
	J1533+0110	15:33:56.00+01:10:29.79	0.14268	on
	J1545+2511	15:45:29.64+25:11:27.87	0.11696	on
	J1550+4139	15:50:17.23+41:39:02.29	0.22014	on
	J1552+2737	15:52:58.30+27:37:28.46	0.08648	on
	J0126-0839	01:26:48.09-08:39:48.05	0.19791	off
	J0159+0033	01:59:57.64+00:33:10.50	0.31204	off
	J1011+5442	10:11:52.99+54:42:06.43	0.24639	off
	J1554+3629	15:54:40.26+36:29:52.01	0.23683	on
	J2336+0017	23:36:02.98+00:17:28.78	0.24283	off
MacLeod et al. (2019)	J0009-1034	00:09:04.54-10:34:28.70	0.241	off
	J0043+1344	00:43:39.33+13:44:36.55	0.527	off
	J0134-0914	01:34:58.36-09:14:35.42	0.443	off
	J0745+3809	07:45:11.98+38:09:11.32	0.236	off
	J0927+0433	09:27:02.30+04:33:08.18	0.322	off
	J1113+5313	11:13:29.68+53:13:38.78	0.239	off
	J1233+0842	12:33:59.13+08:42:11.64	0.25488	off
	J1434+5723	14:34:55.31+57:23:45.10	0.174	off
	J1536+0342	15:36:12.80+03:42:45.85	0.365	off
	J1537+4613	15:37:34.07+46:13:58.95	0.378	off
	J1601+4745	16:01:11.26+47:45:09.69	0.297	off
	J1617+0638	16:17:11.42+06:38:33.50	0.229	off
	J1617+0638	16:17:11.42+06:38:33.50	0.229	off
	J2102+0005	21:02:00.43+00:05:01.92	0.329	off

Table 6. Summary of CLAGN Sources (Continued)

Reference	Name	Coordinate	Redshift	Phase
MacLeod et al. (2019)	J2205-0711	22:05:37.72-07:11:14.58	0.295	off
	J2252+0109	22:52:40.37+01:09:58.71	0.533515	on-off
	J2351-0913	23:51:07.44-09:13:17.90	0.354	off
Frederick et al. (2019)	J0817+1012	08:17:26.42+10:12:10.14	0.045841	LINER-quasar
	J0915+4814	09:15:31.53+48:14:12.26	0.100518	LINER-quasar
	J1133+6701	11:33:55.95+67:01:07.09	0.039757	LINER-Sy1
	J1225+5108	12:25:50.31+51:08:46.38	0.168017	LINER-quasar
	J1254+4914	12:54:03.78+49:14:52.84	0.066947	LINER-quasar
	J1533+4432	15:33:08.01+44:32:08.40	0.036743	LINER-NLS1
Sheng et al. (2020)	J1252+5918	12:52:58.72+59:18:32.76	0.124	off; also WISE1&WISE2 off
	J1307+4506	13:07:16.99+45:06:45.28	0.084	off; also WISE1&WISE2 off
	J1317+1024	13:17:37.92+10:24:27.81	0.28	off; also WISE1&WISE2 off
	J1428+1723	14:28:46.71+17:23:53.11	0.104	off; also WISE1&WISE2 off
	J1627+5419	16:27:52.19+54:19:12.48	0.316	off; also WISE1&WISE2 off
	J1713+2736	17:13:53.85+27:36:27.03	0.298	off; also WISE1&WISE2 off
Potts & Villforth (2021)	J0823+4220	08:23:23.89+42:20:48.30	0.152	off
	J1723+5504	17:23:22.31+55:04:13.80	0.295	on
	J0829+4154	08:29:42.67+41:54:36.90	0.126	on
	J0002-0027	00:02:36.25-00:27:24.80	0.291	off-on
López-Navas et al. (2022)	J0010+0008	00:10:14.89+00:08:20.83	0.1022	on
	J0113+0135	01:13:11.82+01:35:42.58	0.2375	on
	J0755+1923	07:55:44.37+19:23:36.31	0.1083	on
	J0812+0715	08:12:40.75+07:15:28.48	0.0849	on
López-Navas et al. (2023)	J1341+3700	13:41:48.78+37:00:47.13	0.2	on
	J1203+6053	12:03:49.21+60:53:17.45	0.07	on
	J1120+3418	11:20:08.69+34:18:45.83	0.04	on
	J0832+3551	08:32:24.29+35:51:35.92	0.14	on
	J0819+3019	08:19:17.51+30:19:35.76	0.1	on
	J1200+1458	12:00:45.49+14:58:03.67	0.11	on
	J1329-0130	13:29:35.86-01:30:34.03	0.08	on
	J1538+4607	15:38:32.66+46:07:35.01	0.2	on
	J1552+2102	15:52:59.94+21:02:46.89	0.17	on
Yang et al. (2023)	J0206-0609	02:06:21.67-06:09:52.56	0.413	off
	J0224-0918	02:24:29.10-09:18:51.70	0.357	off
	J0829+4202	08:29:05.98+42:02:04.20	0.638	off
	J1226-0011	12:26:38.66-00:11:13.99	0.642	off
Zeltyn et al. (2024)	J0007+0058	00:07:50.51+00:58:15.20	0.345113	on
	J0011+0100	00:11:03.49+01:00:32.62	0.485892	off
	J0038+0002	00:38:41.53+00:02:26.70	0.649649	off
	J0044-0106	00:44:59.09-01:06:29.30	0.228215	off
	J0046+0002	00:46:16.68+00:02:49.09	0.4531	on
	J0115+0033	01:15:36.11+00:33:52.42	0.364029	on
	J0122-0002	01:22:56.19-00:02:52.58	0.340502	on
	J0125+0019	01:25:24.66+00:19:35.90	1.662356	off
	J0129+1504	01:29:46.72+15:04:57.29	0.364851	off
	J0139-0042	01:39:44.05-00:42:51.52	0.471326	off
	J0141+0037	01:41:28.85+00:37:12.22	0.814749	off
	J0142-0050	01:42:09.02-00:50:49.99	0.132549	on
	J0151-0034	01:51:05.80-00:34:26.40	0.335108	off
	J0159+0033	01:59:57.64+00:33:10.51	0.31205	off

Table 7. Summary of CLAGN Sources (Continued)

Reference	Name	Coordinate	Redshift	Phase
Zeltyn et al. (2024)	J0206-0414	02:06:49.48-04:14:52.69	0.138743	off
	J0221-0441	02:21:05.64-04:41:01.50	0.198636	on
	J0239-0044	02:39:04.10-00:44:10.79	0.567837	off
	J0245+0037	02:45:08.68+00:37:10.70	0.29935	off
	J0759+3221	07:59:34.95+32:21:43.31	0.26888	on
	J0801+3417	08:01:33.29+34:17:37.61	0.337982	off
	J0807+1944	08:07:11.72+19:44:39.70	0.347745	off
	J0807+2517	08:07:17.58+25:17:58.70	0.383252	off
	J0810+2116	08:10:09.62+21:16:25.79	0.769466	off
	J0813+2153	08:13:38.47+21:53:49.88	0.548448	off
	J0815+3843	08:15:37.56+38:43:03.22	0.506738	on
	J0820+3441	08:20:18.50+34:41:40.99	0.497461	off
	J0834+2701	08:34:14.18+27:01:01.60	1.071886	off
	J0841+0358	08:41:58.34+03:58:51.71	0.696807	on
	J0845-0027	08:45:28.72-00:27:23.29	0.154388	off
	J0846+0000	08:46:37.65+00:00:24.52	0.257489	off
	J0849+0020	08:49:24.70+00:20:49.70	0.508254	on
	J0853+0143	08:53:37.26+01:43:03.61	0.058189	off
	J0855+0329	08:55:12.13+03:29:50.60	0.124046	off
	J0902+0154	09:02:54.12+01:54:29.09	0.166121	on
	J0903+0106	09:03:15.11+01:06:23.11	0.121657	off
	J0905-0040	09:05:35.77-00:40:39.90	0.793011	off
	J0905+0039	09:05:50.30+00:39:48.10	0.354041	off
	J0906+0144	09:06:12.02+01:44:12.01	0.588482	on
	J0908+0021	09:08:26.74+00:21:37.40	0.162574	on
	J0916+0000	09:16:49.41+00:00:31.61	0.222549	off
	J0923+0434	09:23:13.53+04:34:45.01	0.65682	on
	J0926-0006	09:26:29.23-00:06:05.69	0.201324	on-off
	J0927+0503	09:27:39.77+05:03:12.60	0.126061	off
	J0929+0015	09:29:57.88+00:15:08.71	0.800271	off
	J0930+0118	09:30:41.65+01:18:42.08	2.396249	off
	J0932+0403	09:32:09.96+04:03:19.91	0.275805	off
	J0933+0101	09:33:22.83+01:01:20.89	0.159933	off
	J0936+0121	09:36:14.70+01:21:05.90	0.302738	off
	J1037+3633	10:37:23.72+36:33:41.62	0.519399	off
	J1125+3039	11:25:36.33+30:39:15.91	0.575978	on
	J1128+5656	11:28:25.59+56:56:46.10	0.615026	on
	J1130+3040	11:30:25.21+30:40:33.71	0.842421	off
	J1131+5818	11:31:18.43+58:18:41.80	0.311977	off
	J1133+5921	11:33:33.82+59:21:52.49	0.486347	on
	J1216+5159	12:16:18.00+51:59:46.10	0.623324	off
	J1324+4802	13:24:57.29+48:02:41.32	0.271847	off
	J1354+5159	13:54:15.55+51:59:25.91	0.319749	off
	J1357+5537	13:57:26.62+55:37:36.01	2.363621	on
	J1357+6143	13:57:50.26+61:43:09.01	0.737404	off
	J1405+5424	14:05:15.59+54:24:58.00	0.083262	on
	J1411+5315	14:11:44.12+53:15:08.60	0.923187	off
	J1426+3212	14:26:13.05+32:12:12.31	0.523328	off
	J1428+0452	14:28:13.06+04:52:47.60	0.445953	off
	J1440+3456	14:40:24.60+34:56:24.22	0.752449	off

Table 8. Summary of CLAGN Sources (Continued)

Reference	Name	Coordinate	Redshift	Phase
Zeltyn et al. (2024)	J1607+5603	16:07:30.23+56:03:05.62	0.717069	on
	J1617+4902	16:17:34.42+49:02:11.90	0.880448	off
	J1628+4329	16:28:29.18+43:29:48.59	0.260285	off
	J1631+3844	16:31:10.02+38:44:57.41	0.583915	off
	J1652+3937	16:52:34.96+39:37:33.38	0.641484	on
	J2118+0053	21:18:34.39+00:53:22.20	0.451338	on
	J2223+1944	22:23:06.32+19:44:31.60	0.259936	off
	J2336+0040	23:36:50.69+00:40:42.49	0.161514	off
Yang et al. (2025)	J0040+1609	00:40:38.40+16:09:49.93	0.2937904	on
	J0047+1541	00:47:30.34+15:41:49.41	0.031420413	on
	J0107+2428	01:07:47.92+24:28:48.70	0.1602249	on
	J0110+0026	01:10:59.31+00:26:01.14	0.018818583	on
	J0132+1501	01:32:42.04+15:01:14.76	0.17000946	on
	J0141+0105	01:41:53.98+01:05:05.50	0.10127	on
	J0146+1311	01:46:38.87+13:11:09.39	0.16013657	on
	J0334+0051	03:34:31.32+00:51:21.37	0.4293435	on
	J0803+2207	08:03:04.74+22:07:34.03	0.12452307	on
	J0813+4608	08:13:19.32+46:08:49.69	0.053826876	on
	J0823+4202	08:23:58.66+42:02:59.21	0.12564875	on
	J0829+2319	08:29:23.00+23:19:32.70	0.1442577	on
	J0837+0356	08:37:16.47+03:56:06.06	0.06348244	on
	J0854+1113	08:54:34.65+11:13:34.78	0.16718863	on
	J0901+2907	09:01:15.02+29:07:34.39	0.2176674	on
	J0906+4046	09:06:12.28+40:46:38.51	0.1669009	on
	J0908+0755	09:08:14.07+07:55:24.27	0.14367613	on
	J0910+1907	09:10:13.70+19:07:01.37	0.18770769	on
	J0914+0502	09:14:59.15+05:02:43.42	0.14251585	on
	J0926-0006	09:26:29.23-00:06:05.72	0.20132396	on
	J0936+2726	09:36:33.56+27:26:04.34	0.10286305	on
	J0947+5449	09:47:46.56+54:49:55.82	0.6195132	on
	J0952+2229	09:52:17.39+22:29:25.76	0.08075754	on
	J1000+0354	10:00:01.81+03:54:02.04	0.21543361	on
	J1002+0303	10:02:07.03+03:03:27.67	0.023351775	on
	J1003+0202	10:03:50.98+02:02:27.65	0.12469647	on
	J1003+0458	10:03:40.39+04:58:20.70	0.12374884	on
	J1009+3539	10:09:06.07+35:39:32.65	0.110079706	on
	J1012+5559	10:12:48.93+55:59:18.44	0.12547755	on
	J1017+0658	10:17:37.94+06:58:16.18	0.045342874	on
	J1058+6338	10:58:53.56+63:38:41.09	0.20183021	on
	J1102+5722	11:02:00.11+57:22:50.50	0.14184508	on
	J1105+0516	11:05:29.70+05:16:49.23	0.091155544	on
	J1110+0804	11:10:00.32+08:04:15.71	0.116119295	on
	J1111+1401	11:11:37.58+14:01:18.15	0.11065613	on
	J1126+0510	11:26:21.87+05:10:02.97	0.17030554	on
	J1149+3351	11:49:26.45+33:51:55.43	0.08091733	on
	J1155+0048	11:55:47.64+00:48:52.00	0.20884128	on
	J1158+1003	11:58:18.01+10:03:22.55	0.06992021	on
	J1159+0513	11:59:53.39+05:13:29.98	0.059330106	on
	J1159+6545	11:59:37.89+65:45:36.56	0.1218518	on
	J1226+4559	12:26:35.48+45:59:32.38	0.10874906	on

Table 9. Summary of CLAGN Sources (Continued)

Reference	Name	Coordinate	Redshift	Phase
Yang et al. (2025)	J1231+3232	12:31:55.14+32:32:40.26	0.06536951	on
	J1239+0739	12:39:24.74+07:39:03.91	0.13254617	on
	J1311+0705	13:11:03.04+07:05:09.73	0.30051038	on
	J1311+4300	13:11:50.35+43:00:25.34	0.28453356	on
	J1327+4025	13:27:23.74+40:25:04.48	0.0777004	on
	J1328+6227	13:28:11.58+62:27:43.16	0.09058887	on
	J1340+4006	13:40:54.65+40:06:37.41	0.17076361	on
	J1341-0049	13:41:05.98-00:49:02.62	0.17537512	on
	J1433+4943	14:33:18.21+49:43:01.29	0.12459213	on
	J1442+5558	14:42:27.58+55:58:46.37	0.07689327	on
	J1611+1642	16:11:13.84+16:42:03.29	0.15476471	on
	J1612+3113	16:12:04.26+31:13:07.86	0.1773024	on
	J1612+3816	16:12:46.01+38:16:43.85	0.19936875	on
	J1636+3930	16:36:51.32+39:30:07.37	0.1818733	on
	J1638+4712	16:38:06.33+47:12:12.67	0.114344485	on
	J1640+2819	16:40:08.44+28:19:53.31	0.18136162	on
	J1642+4423	16:42:38.27+44:23:31.62	0.22664222	on
	J1643+5000	16:43:47.13+50:00:50.38	0.060020957	on
	J1652+3416	16:52:21.38+34:16:41.70	0.26308012	on
	J2120-0056	21:20:39.75-00:56:44.29	0.25076804	on
	J2150-0106	21:50:55.73-01:06:54.19	0.08790665	on
	J2156+2907	21:56:43.84+29:07:57.96	0.091868415	on
	J2159+0556	21:59:05.79+05:56:39.46	0.1109222	on
	J2201+0352	22:01:50.84+03:52:11.54	0.135897	on
	J2203+1124	22:03:49.23+11:24:32.99	0.18626842	on
	J2320+1448	23:20:10.99+14:48:15.15	0.08222562	on
	J2336+1514	23:36:13.90+15:14:56.32	0.14734927	on
	J2348+0741	23:48:54.90+07:41:36.68	0.46374503	on

Facilities: Sloan, ZTF

Software: astropy (Astropy Collaboration et al. 2013, 2018), astroquery (Ginsburg et al. 2019), pandas (The pandas development Team 2024), `qso_fit` (Butler & Bloom 2011), TOPCAT (Taylor 2005)

REFERENCES

Astropy Collaboration, Robitaille, T. P., Tollerud, E. J., et al. 2013, A&A, 558, A33, doi: 10.1051/0004-6361/201322068

Astropy Collaboration, Price-Whelan, A. M., Sipőcz, B. M., et al. 2018, AJ, 156, 123, doi: 10.3847/1538-3881/aabc4f

Becker, R. H., White, R. L., & Helfand, D. J. 1995, ApJ, 450, 559, doi: 10.1086/176166

Butler, N. R., & Bloom, J. S. 2011, AJ, 141, 93, doi: 10.1088/0004-6256/141/3/93

Calzetti, D. 2001, PASP, 113, 1449, doi: 10.1086/324269

Cui, X.-Q., Zhao, Y.-H., Chu, Y.-Q., et al. 2012, Research in Astronomy and Astrophysics, 12, 1197, doi: 10.1088/1674-4527/12/9/003

DESI Collaboration, Abdul-Karim, M., Adame, A. G., et al. 2025, arXiv e-prints, arXiv:2503.14745, doi: 10.48550/arXiv.2503.14745

Dong, Q., Zhang, Z.-X., Gu, W.-M., Sun, M., & Zheng, Y.-G. 2025, ApJ, 986, 160, doi: 10.3847/1538-4357/add331

Ferrarese, L. 2002, ApJ, 578, 90, doi: 10.1086/342308

Flesch, E. W. 2021, The Million Quasars (Milliquas) v7.2 Catalogue, now with VLASS associations. The inclusion of SDSS-DR16Q quasars is detailed. https://arxiv.org/abs/2105.12985

Frederick, S., Gezari, S., Graham, M. J., et al. 2019, ApJ, 883, 31, doi: 10.3847/1538-4357/ab3a38

Ginsburg, A., Sipőcz, B. M., Brasseur, C. E., et al. 2019, AJ, 157, 98, doi: 10.3847/1538-3881/aafc33

Graham, M. J., Ross, N. P., Stern, D., et al. 2020, MNRAS, 491, 4925, doi: 10.1093/mnras/stz3244

Guo, W.-J., Zou, H., Fawcett, V. A., et al. 2024, ApJS, 270, 26, doi: 10.3847/1538-4365/ad118a

Guo, W.-J., Zou, H., Greenwell, C. L., et al. 2025, ApJS, 278, 28, doi: 10.3847/1538-4365/adc124

Hagen, S., Done, C., Silverman, J. D., et al. 2024, MNRAS, 534, 2803, doi: 10.1093/mnras/stae2272

Hawkins, M. R. S. 2004, A&A, 424, 519, doi: 10.1051/0004-6361:20041127

Hopkins, P. F., Richards, G. T., & Hernquist, L. 2007, ApJ, 654, 731, doi: 10.1086/509629

Jana, A., Ricci, C., Temple, M. J., et al. 2025, A&A, 693, A35, doi: 10.1051/0004-6361/202451058

Jin, J.-J., Wu, X.-B., & Feng, X.-T. 2022, ApJ, 926, 184, doi: 10.3847/1538-4357/ac410c

Kelly, B. C., Bechtold, J., & Siemiginowska, A. 2009, ApJ, 698, 895, doi: 10.1088/0004-637X/698/1/895

Kim, M., Son, S., & Ho, L. C. 2024, A&A, 689, A27, doi: 10.1051/0004-6361/202450413

Kovacevic, N., Dai, X., Yuk, H., et al. 2025, ApJ, 985, 177, doi: 10.3847/1538-4357/adcb40

Kozłowski, S. 2016, ApJ, 826, 118, doi: 10.3847/0004-637X/826/2/118

LaMassa, S. M., Yaqoob, T., Ptak, A. F., et al. 2014, ApJ, 787, 61, doi: 10.1088/0004-637X/787/1/61

LaMassa, S. M., Cales, S., Moran, E. C., et al. 2015, ApJ, 800, 144, doi: 10.1088/0004-637X/800/2/144

López-Navas, E., Martínez-Aldama, M. L., Bernal, S., et al. 2022, MNRAS, 513, L57, doi: 10.1093/mnrasl/slac033

López-Navas, E., Sánchez-Sáez, P., Arévalo, P., et al. 2023, MNRAS, 524, 188, doi: 10.1093/mnras/stad1893

Lyke, B. W., Higley, A. N., McLane, J. N., et al. 2020, ApJS, 250, 8, doi: 10.3847/1538-4365/aba623

Lyu, B., Yan, Z., Wu, X.-b., et al. 2025, MNRAS, 537, 1099, doi: 10.1093/mnras/staf109

MacLeod, C. L., Ivezić, Ž., Sesar, B., et al. 2012, ApJ, 753, 106, doi: 10.1088/0004-637X/753/2/106

MacLeod, C. L., Ross, N. P., Lawrence, A., et al. 2016, MNRAS, 457, 389, doi: 10.1093/mnras/stv2997

MacLeod, C. L., Green, P. J., Anderson, S. F., et al. 2019, ApJ, 874, 8, doi: 10.3847/1538-4357/ab05e2

Masci, F. J., Laher, R. R., Rusholme, B., et al. 2019, PASP, 131, 018003, doi: 10.1088/1538-3873/aae8ac

Mereghetti, S., Balman, S., Caballero-Garcia, M., et al. 2021, Experimental Astronomy, 52, 309, doi: 10.1007/s10686-021-09809-6

Noda, H., & Done, C. 2018, MNRAS, 480, 3898, doi: 10.1093/mnras/sty2032

Panessa, F., Carrera, F. J., Bianchi, S., et al. 2009, MNRAS, 398, 1951, doi: 10.1111/j.1365-2966.2009.15225.x

Pâris, I., Petitjean, P., Aubourg, É., et al. 2018, A&A, 613, A51, doi: 10.1051/0004-6361/201732445

Pennell, A., Runnoe, J. C., & Brotherton, M. S. 2017, MNRAS, 468, 1433, doi: 10.1093/mnras/stx556

Potts, B., & Villforth, C. 2021, A&A, 650, A33, doi: 10.1051/0004-6361/202140597

Ren, W., Wang, J., Cai, Z., & Guo, H. 2022, ApJ, 925, 50, doi: 10.3847/1538-4357/ac3828

Ricci, C., & Trakhtenbrot, B. 2023, Nature Astronomy, 7, 1282, doi: 10.1038/s41550-023-02108-4

Schmidt, K. B., Marshall, P. J., Rix, H.-W., et al. 2010, ApJ, 714, 1194, doi: 10.1088/0004-637X/714/2/1194

Sheng, Z., Wang, T., Jiang, N., et al. 2020, ApJ, 889, 46, doi: 10.3847/1538-4357/ab5af9

Tang, J.-J., Wolf, C., & Tonry, J. 2023, Nature Astronomy, 7, 473, doi: 10.1038/s41550-022-01885-8

Taylor, M. B. 2005, in Astronomical Society of the Pacific Conference Series, Vol. 347, Astronomical Data Analysis Software and Systems XIV, ed. P. Shopbell, M. Britton, & R. Ebert, 29

The pandas development Team. 2024, pandas-dev/pandas: Pandas, v2.2.3, Zenodo, doi: 10.5281/zenodo.3509134

Thomas, D., Steele, O., Maraston, C., et al. 2013, MNRAS, 431, 1383, doi: 10.1093/mnras/stt261

Urry, C. M., & Padovani, P. 1995, PASP, 107, 803, doi: 10.1086/133630

van Velzen, S., Holoien, T. W. S., Onori, F., Hung, T., & Arcavi, I. 2020, SSRv, 216, 124, doi: 10.1007/s11214-020-00753-z

Vanden Berk, D. E., Wilhite, B. C., Kron, R. G., et al. 2004, ApJ, 601, 692, doi: 10.1086/380563

Vestergaard, M., & Peterson, B. M. 2006, ApJ, 641, 689, doi: 10.1086/500572

Wang, S., Woo, J.-H., Gallo, E., et al. 2024, ApJ, 966, 128, doi: 10.3847/1538-4357/ad3049

Wu, Q., & Shen, Y. 2022, ApJS, 263, 42, doi: 10.3847/1538-4365/ac9ead

Yang, Q., Green, P. J., Wu, X.-B., et al. 2025, ApJ, 980, 91, doi: 10.3847/1538-4357/ad94ed

Yang, Q., Wu, X.-B., Fan, X., et al. 2018, ApJ, 862, 109, doi: 10.3847/1538-4357/aaca3a

Yang, Q., Green, P. J., MacLeod, C. L., et al. 2023, ApJ, 953, 61, doi: 10.3847/1538-4357/acdedd

Zeltyn, G., Trakhtenbrot, B., Eracleous, M., et al. 2024, ApJ, 966, 85, doi: 10.3847/1538-4357/ad2f30

Zhu, L.-T., Wang, Z., Devanand, P. U., et al. 2025, MNRAS, 536, 2715, doi: 10.1093/mnras/stae2774